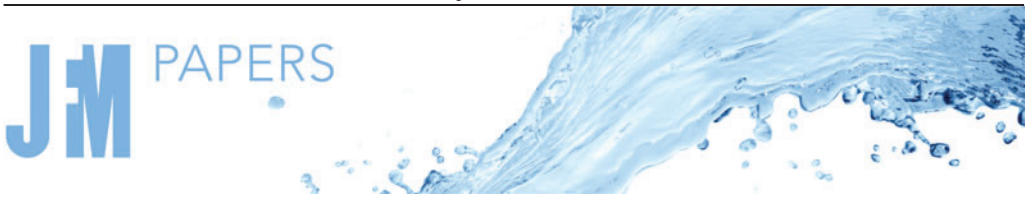
J. Fluid Mech. (2022), *vol*. 939, A16, doi:10.1017/jfm.2022.213



On shock-induced evolution of a gas layer with two fast/slow interfaces

Yu Liang[1,2] **and Xisheng Luo**[1,†]

[1]Advanced Propulsion Laboratory, Department of Modern Mechanics, University of Science and Technology of China, Hefei 230026, PR China

[2]NYUAD Research Institute, New York University Abu Dhabi, Abu Dhabi 129188, UAE

(Received 9 October 2021; revised 15 January 2022; accepted 6 March 2022)

The shock-induced evolution of a gas layer with two fast/slow interfaces is investigated theoretically and experimentally. Specifically, the gas layer is located between a lighter gas and a heavier gas, forming a light/medium/heavy (LMH) configuration. Linear stability analysis is utilised to derive a new analytical model to quantify the Richtmyer–Meshkov instability (RMI) on the two interfaces of such an A/B/C-type fluid layer. Three quasi-one-dimensional (1-D) LMH fluid layers with different initial layer thicknesses are generated to study the wave patterns and interface motions. A general 1-D theory is established to describe the motions of the shock/rarefaction waves reverberating inside the fluid layer and the displacements of the two interfaces. Six quasi-2-D LMH fluid layers with diverse initial layer-thickness and amplitude combinations are created to explore the hydrodynamic instabilities of the two interfaces. It is found that the interface coupling significantly influences the interface evolution, even resulting in an abnormal phase reversal of a shocked fast/slow interface if the two interfaces are anti-phase and the initial layer is very thin. The specific conditions for the abnormal phase reversal and the instability freeze out are deduced. Moreover, the additional RMI (or Rayleigh–Taylor stabilisation) imposed by the shock (or rarefaction waves) reverberating inside an LMH fluid layer on the first (or second) interface is quantified. It is proved that the reverberating waves inside an LMH fluid layer stabilise the two interfaces. Finally, a nonlinear model is obtained by incorporating the nonlinearity effect into the linear model, which well describes the perturbation growths of the two interfaces in a later regime.

Key words: shock waves

† Email address for correspondence: xluo@ustc.edu.cn

© The Author(s), 2022. Published by Cambridge University Press

https://doi.org/10.1017/jfm.2022.213 Published online by Cambridge University Press

1. Introduction

Richtmyer–Meshkov instability (RMI) occurs when a shock wave impacts on an interface between two fluids with different densities (Richtmyer 1960; Meshkov 1969), and then induces finger-like flow structures such as the bubble (light fluid penetrating heavy one) and the spike (heavy fluid penetrating light one). It finally may cause a flow transition to turbulent mixing (Zhou *et al.* 2019). Over the past decades, RMI has become a subject of intensive research due to its crucial role in various industrial and scientific fields such as inertial confinement fusion (ICF) (Lindl *et al.* 2014), supersonic combustion (Yang, Kubota & Zukoski 1993), supernova explosions (Kuranz *et al.* 2018) and ejecta, material strength, chemical reactions, solar prominences and ionospheric flows (Zhou *et al.* 2021). The RMI on a semi-infinite single-mode interface that has the simplest mathematical form has been extensively studied (Brouillette 2002; Zhou 2017*a*,*b*; Zhai *et al.* 2018). However, RMI is generally involved in the issue of the multi-interface evolution. For example, RMI is initiated when the shocks generated by intense lasers or X-rays interact with the outer ablator layer, the middle push layer and the inner fuel layer of an ICF capsule. The mixing induced by RMI significantly reduces and even eliminates the thermonuclear yield. In addition, RMI occurs when the shocks generated by star collapse in a supernova interact with continuous multi-layer heavy elements throughout the interstellar space. The mixing induced by RMI shapes the filament structures in the supernova remnant. Therefore, it is significant to investigate the mixing caused by the RMI in a multi-interface system.

Most previous studies considered the RMI of an A/B/A-type fluid layer, i.e. two interfaces separating two kinds of fluids (gas A and gas B). Theoretically, the linear solutions for the amplitude growth rates of the two interfaces of an A/B/A-type fluid layer were separately derived by Jacobs *et al.* (1995) and Mikaelian (1985, 1995, 1996). As the initial layer thickness reduces, the interface-coupling effect on the RMI is more prominent. Experimentally, the gas curtain technology was mainly adopted to explore the RMI of a thin SF_6 layer surrounded by air. It was found that the shock-induced morphologies of the SF_6 layer are sensitive to the initial shape of the layer (Jacobs *et al.* 1993; Budzinski, Benjamin & Jacobs 1994; Jacobs *et al.* 1995; Rightley, Vorobieff & Benjamin 1997), and the late-time mixing is influenced by initial conditions such as the perturbation amplitude and wavelength of the fluid layer, the incident shock strength, etc. (Prestridge *et al.* 2000; Tomkins *et al.* 2008; Balakumar *et al.* 2008; Orlicz *et al.* 2009; Balakumar *et al.* 2012; Orlicz, Balasubramanian & Prestridge 2013; Tomkins *et al.* 2013). The soap film technique was recently utilised to generate an SF_6 gas layer surrounded by air (Ding *et al.* 2019; Liang *et al.* 2020*a*; Li *et al.* 2020; Sun *et al.* 2020; Liang & Luo 2021*a*,*b*). It was determined that the waves reverberating inside a fluid layer induce various interfacial instabilities at the two sides of the fluid layer. For instance, the rarefaction waves inside an SF_6 layer impose the additional Rayleigh–Taylor instability (Rayleigh 1883; Taylor 1950) on the first interface, and the compression waves inside an SF_6 layer impose additional Rayleigh–Taylor stabilisation (RTS) on the second interface (Liang & Luo 2021*a*). Differently, the reflected shocks reverberating inside a helium layer induce the additional RMI on the two interfaces (Liang & Luo 2022).

On comparing with an A/B/A-type fluid layer, an A/B/C-type fluid layer, i.e. two interfaces separating three kinds of fluids (fluids A, B and C), is more general in its applications. For example, the double-shell ICF capsule consists of a CH form shell ($35\,\mathrm{mg\,ml^{-1}}$) between the outer shell ($2.7\,\mathrm{g\,ml^{-1}}$) and the inner shell ($200\,\mathrm{mg\,ml^{-1}}$) (Montgomery *et al.* 2018; Haines *et al.* 2021). The materials in various shells are entirely different. Moreover, the waves reverberating inside an A/B/C-type fluid layer are quite

https://doi.org/10.1017/jfm.2022.213 Published online by Cambridge University Press

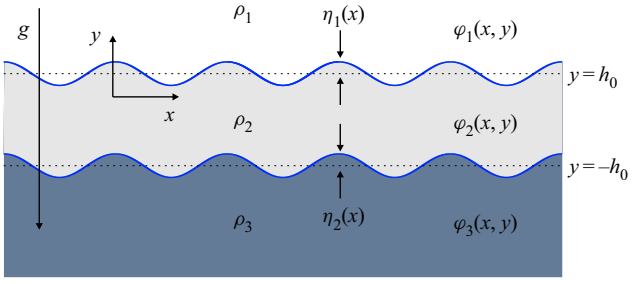


Figure 1. Schematic showing the configuration analysed using linear stability theory for a more general system of three incompressible and initially irrotational fluids, where ρ_1, ρ_2 and ρ_3 are the densities of the three fluids, and ϕ_1, ϕ_2 and ϕ_3 are the velocity potentials; η_1 and η_2 are initial perturbations and $2h_0$ is the initial layer thickness.

different from those inside an A/B/A-type fluid layer. As a result, it is expected that the influences of the reverberating waves on the two interfaces of a fluid layer are dissimilar under the A/B/C-type and A/B/A-type fluid-layer conditions. Moreover, designing an appropriate layer thickness could be used advantageously to minimise the mixing in ICF capsules (Drake 2018). However, theoretical solutions and experiments on the RMI of an A/B/C-type fluid layer with variant layer thicknesses are still lacking.

In this work, we first derive a new linear model by considering the interface-coupling effect to evaluate the amplitude growth rates of the two interfaces of an A/B/C-type fluid layer in the weak-shock limit. Then, we extend the soap film technique to generate a fluid layer with two fast/slow interfaces, i.e. the fluid layer is located between a semi-infinite lighter gas and a semi-infinite heavier gas, which forms a light/medium/heavy (LMH) configuration. The lightest gas is air, the medium gas is a mixture of air and SF_6 (at moderate concentration) and the heaviest gas is a mixture of air and SF_6 (at high concentration). Later, we elaborate shock-tube experiments on three quasi-one-dimensional (quasi-1-D) LMH fluid layers with various layer thicknesses that are performed to investigate the wave patterns and interface motions. Further, shock-tube experiments on six quasi-two-dimensional (quasi-2-D) LMH fluid layers with different layer thickness and amplitude combinations are conducted to investigate the hydrodynamic instabilities of the two interfaces. Finally, the linear model is extended to a nonlinear one by considering the nonlinearity effect to describe the perturbation growths of the two interfaces in a later regime.

2. Linear stability analysis

We first perform a linear stability analysis to acquire the theoretical amplitude growth rates of the first interface ($\dot{a}_1^l$) and the second interface ($\dot{a}_2^l$) of an A/B/C-type fluid layer by considering the interface-coupling effect. Different from the previous analysis on an A/B/A-type fluid layer (Jacobs *et al.* 1995; Mikaelian 1996), we consider a more general system of three incompressible and initially irrotational fluids of densities ρ_1, ρ_2 and ρ_3, and velocity potentials ϕ_1, ϕ_2 and ϕ_3, separated by two nearly planar interfaces with perturbations η_1 and η_2 and an initial layer thickness of $2h_0$, as sketched in figure 1.

The equations that govern the growth of infinitesimal disturbances on the boundaries of the layer are

$$\nabla^2\phi = 0, \tag{2.1}$$

https://doi.org/10.1017/jfm.2022.213 Published online by Cambridge University Press

in each of the three fluids, with the kinematic conditions on $y = \pm h_0$,

$$\frac{\partial \eta}{\partial t} - \frac{\partial \phi}{\partial y} = 0, \tag{2.2}$$

and the conditions of the pressure equilibrium on $y = \pm h_0$,

$$\rho \frac{\partial \phi}{\partial t} - \rho g \eta + p = P_0, \tag{2.3}$$

where p is pressure, g is the acceleration and P_0 is a constant and equals the pressure at an unperturbed interface. Periodic perturbation amplitudes set on the first interface (a_1) and the second interface (a_2) are of the form

$$\eta_1 = a_1(t)\cos(kx), \quad \eta_2 = a_2(t)\cos(kx), \tag{2.4a,b}$$

then requires the following velocity potentials in the three fluids (Jacobs *et al.* 1995):

$$\left.\begin{aligned} \phi_1 &= b_1(t)\mathrm{e}^{-k(y-h_0)}\cos(kx), \\ \phi_2 &= -\left[\frac{b_1+b_2}{2}\frac{\sinh(ky)}{\cosh(kh_0)} + \frac{b_1-b_2}{2}\frac{\cosh(ky)}{\sinh(kh_0)}\right]\cos(kx), \\ \phi_3 &= -b_2(t)\mathrm{e}^{k(y+h_0)}\cos(kx). \end{aligned}\right\} \tag{2.5}$$

Substituting (2.4*a*,*b*) and (2.5) into (2.2) and (2.3) yields

$$\frac{\mathrm{d}a_1}{\mathrm{d}t} = -kb_1, \tag{2.6}$$

$$\frac{\mathrm{d}a_2}{\mathrm{d}t} = -kb_2, \tag{2.7}$$

$$[\rho_1 + \rho_2\tanh(kh_0)]\frac{\mathrm{d}b_1}{\mathrm{d}t} + [\rho_3 + \rho_2\tanh(kh_0)]\frac{\mathrm{d}b_2}{\mathrm{d}t} = g\left[(\rho_1-\rho_2)a_1 + (\rho_2-\rho_3)a_2\right], \tag{2.8}$$

$$[\rho_1 + \rho_2\coth(kh_0)]\frac{\mathrm{d}b_1}{\mathrm{d}t} - [\rho_3 + \rho_2\coth(kh_0)]\frac{\mathrm{d}b_2}{\mathrm{d}t} = g\left[(\rho_1-\rho_2)a_1 + (\rho_3-\rho_2)a_2\right]. \tag{2.9}$$

Equations (2.6)–(2.9) can be combined to yield a pair of ordinary differential equations for a_1 and a_2

$$[\rho_1 + \rho_2\tanh(kh_0)]\frac{\mathrm{d}^2a_1}{\mathrm{d}t^2} + [\rho_3 + \rho_2\tanh(kh_0)]\frac{\mathrm{d}^2a_2}{\mathrm{d}t^2} = kg\left[(\rho_2-\rho_1)a_1 + (\rho_3-\rho_2)a_2\right], \tag{2.10}$$

$$[\rho_1 + \rho_2\coth(kh_0)]\frac{\mathrm{d}^2a_1}{\mathrm{d}t^2} - [\rho_3 + \rho_2\coth(kh_0)]\frac{\mathrm{d}^2a_2}{\mathrm{d}t^2} = kg\left[(\rho_2-\rho_1)a_1 + (\rho_2-\rho_3)a_2\right]. \tag{2.11}$$

For RMI, the acceleration g can be replaced by the jump speed of a fluid layer (Δv) and a Dirac delta function (i.e. $g = \Delta v\delta t$ with $\delta t = 0$ when $t = 0$ and $\delta t = 1$ when $t > 0$)

https://doi.org/10.1017/jfm.2022.213 Published online by Cambridge University Press

allowing (2.10) and (2.11) to be easily integrated in the weak-shock limit. Thus,

$$[\rho_1 + \rho_2 \tanh(kh_0)]\,\dot{a}_1^l + [\rho_3 + \rho_2 \tanh(kh_0)]\,\dot{a}_2^l = k\Delta v\,[(\rho_2 - \rho_1)a_1(0) + (\rho_3 - \rho_2)a_2(0)]\,, \tag{2.12}$$

$$[\rho_1 + \rho_2 \coth(kh_0)]\,\dot{a}_1^l - [\rho_3 + \rho_2 \coth(kh_0)]\,\dot{a}_2^l = k\Delta v\,[(\rho_2 - \rho_1)a_1(0) + (\rho_2 - \rho_3)a_2(0)]\,. \tag{2.13}$$

There are a few linear models considering different post-shock parameter combinations to evaluate the compression effect induced by the incident shock (Richtmyer 1960; Meyer & Blewett 1972; Fraley 1986; Vandenboomgaerde, Mügler & Gauthier 1998). In this study, we shall follow the original prescriptions introduced by Richtmyer (1960) since the Richtmyer model has the most simplified form sufficient to quantify the linear amplitude growth rate of a fast/slow interface in the weak-shock limit. Replacing the pre-shock parameters in (2.12) and (2.13) with the post-shock parameters of the two interfaces, $\dot{a}_1^l$ and $\dot{a}_2^l$ can be separately solved as

$$\dot{a}_1^l = -\frac{k\Delta v_1 Z_1 a_1(0)\left[(R_1 - 1)(2R_3\xi + \xi^2 + 1) + (1 - R_3)(1 - \xi^2)/\epsilon\right]}{2\xi(R_1R_3 + 1) + (R_1 + R_3)(\xi^2 + 1)}, \tag{2.14}$$

$$\dot{a}_2^l = \frac{k\Delta v_2 Z_2 a_2(0)\left[\epsilon(R_1 - 1)(\xi^2 - 1) - (1 - R_3)(2R_1\xi + \xi^2 + 1)\right]}{2\xi(R_1R_3 + 1) + (R_1 + R_3)(\xi^2 + 1)}, \tag{2.15}$$

in which Δv_1 denotes the velocity jump of the first interface induced by the incident shock (IS), Δv_2 denotes the velocity jump of the second interface induced by the transmitted shock inside the fluid layer (TS_1); Z_1 $(= 1 - \Delta v_1/v_{IS})$ and Z_2 $(= 1 - \Delta v_1/v_{TS_1})$ are compression factors with v_{IS} and v_{TS_1} denoting the speed of the IS and the TS_1, respectively; $\xi = \tanh(Z_L kh_0)$, $Z_L = 1 - \Delta v_1/v_{TS_1}$, $R_1 = \rho_1/\rho_2$, $R_3 = \rho_3/\rho_2$ and $\epsilon = Z_1a_1(0)/Z_2a_2(0)$. Here, (2.14) and (2.15) are called the LL model. Notably, the LL model is also applicable to an A/B/A-type fluid layer when $R_1 = R_3$.

3. Experimental method

The soap film technique is extended to generate two shape-controllable and discontinuous interfaces of an LMH fluid layer, mainly eliminating the additional short-wavelength perturbations, diffusion layer and three-dimensionality (Liu *et al.* 2018; Liang *et al.* 2019; Luo *et al.* 2020; Liang *et al.* 2021). As shown in figure 2(*a*), three transparent devices (i.e. left device, middle device and right device) with a width of 140.0 mm and a height of 10.0 mm are first manufactured using transparent acrylic sheets with a thickness of 3.0 mm. The middle device's adjacent boundaries are carefully engraved to be of a sinusoidal shape with a depth of 1.8 mm. Then, four thin filaments (marked green in figure 2*a*) with a height of 2.0 mm are attached to the upper and lower plates' inner surfaces at two sides of the middle device to restrict the soap film's shape. Thus the filament bulges in the flow field with only 0.2 mm height. Before the interface formation, the filaments are properly wetted by a soap solution with a mass fraction of 78 % distilled water, 2 % sodium oleate and 20 % glycerine.

First, a small rectangular frame with moderate soap solutions dipped on its borders is pulled along the sinusoidal filaments on both sides of the middle device. Two soap film interfaces are formed, and the middle device is closed. Second, SF_6 is pumped into the closed space through an inflow hole to discharge air inside through an outflow hole.

https://doi.org/10.1017/jfm.2022.213 Published online by Cambridge University Press

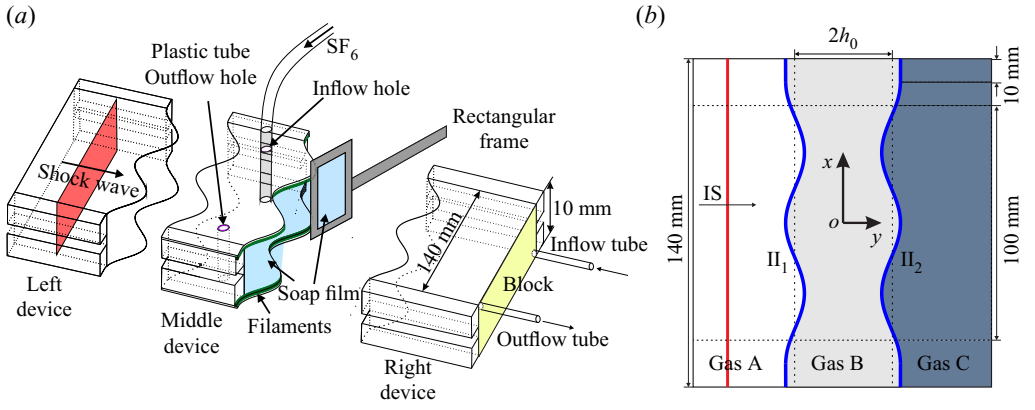


Figure 2. Schematics of (*a*) the soap film interface generation and (*b*) the initial configuration studied in the present work, where h_0 denotes half of the initial layer thickness, II_1 denotes the first initial interface and II_2 denotes the second initial interface.

An oxygen concentration detector is placed at the outflow hole to monitor the concentration of SF_6 inside the closed space. Third, when the volume fraction of oxygen at the outflow hole reduces to 10 %, both the inflow and outflow holes are sealed. Fourth, the left and right transparent devices are gently connected to the middle device, and the combined one is inserted into the open-ended test section of a shock tube. Fifth, the end of the right device is sealed with a block. Then, SF_6 is injected into the right device through an inflow tube at the right bottom corner of the block, and the air is exhausted through an outflow tube at the left top corner of the block. In the meantime, the oxygen concentration detector is placed at the end of the outflow tube to monitor the concentration of SF_6 inside the right device. Sixth, the inflow and outflow tubes are sealed when the detected oxygen concentration decreases to around 0.02 %. Finally, shock-tube experiments are conducted as soon as possible to reduce gas diffusion among the various devices.

In the Cartesian coordinate system, as sketched in figure 2(*b*), the initial perturbations on the nth interface are single mode as $y = a_n(0)\cos(kx + \pi)$ within the range of $x \in [-60.0, 60.0]$ mm, where k denotes the wavenumber of the two interfaces. In this work, $k = 104.7\ \mathrm{m}^{-1}$; $a_1(0)$ and $a_2(0)$ in all cases are listed in table 1. To minimise the wall effect of the shock tube on the interface evolution, a short flat part with 10.0 mm on each side of the two interfaces is adopted. Its influence on the interface evolution is limited (Luo *et al.* 2019). The initial layer thickness ($2h_0$) is defined as the distance between the average positions of the first initial interface (II_1) and the second initial interface (II_2). Overall, we shall investigate three quasi-1-D LMH fluid layers with no perturbations and six quasi-2-D LMH fluid layers with three initial layer thicknesses and two amplitude combinations. Here, we define the three cases (i.e. cases L10-IP, L30-IP and L50-IP) with $a_2(0) > 0$ as in-phase cases and the three cases (i.e. cases L10-AP, L30-AP and L50-AP) with $a_2(0) < 0$ as anti-phase cases. As sketched in figure 2(*b*), gas A (light gas) is air, gas B (medium gas) is a mixture of air and SF_6 (with a moderate mass fraction MF_B) and gas C (heavy gas) is a mixture of air and SF_6 (with a high mass fraction MF_C). The Atwood number of the first interface is A_1 ($= (\rho_B - \rho_A)/(\rho_B + \rho_A)$, with ρ_A denoting the density of gas A and ρ_B denoting the density of gas B), and the Atwood number of the second interface is A_2 ($= (\rho_C - \rho_B)/(\rho_C + \rho_B)$, with ρ_C denoting the density of gas C), respectively. The values of MF_B, MF_C, A_1 and A_2 are listed in table 1.

https://doi.org/10.1017/jfm.2022.213 Published online by Cambridge University Press

Case	L10-1D	L30-1D	L50-1D	L10-IP	L10-AP	L30-IP	L30-AP	L50-IP	L50-AP
$a_1(0)$ (mm)	0	0	0	2.0	2.0	2.0	2.0	2.0	2.0
$a_2(0)$ (mm)	0	0	0	2.0	−2.0	2.0	−2.0	2.0	−2.0
$2h_0$ (mm)	10.0	30.0	50.0	10.0	10.0	30.0	30.0	50.0	50.0
MF_B	0.86	0.86	0.87	0.84	0.86	0.82	0.82	0.79	0.81
MF_C	0.94	0.93	0.95	0.95	0.95	0.97	0.91	0.89	0.96
A_1	0.53	0.53	0.53	0.50	0.53	0.48	0.48	0.46	0.48
A_2	0.19	0.18	0.19	0.22	0.19	0.25	0.21	0.23	0.25

Table 1. Physical parameters of a LMH fluid layer, where $a_1(0)$ ($a_2(0)$) denotes the initial amplitude of the first (second) interface, h_0 denotes half of the initial layer thickness, MF_B (MF_C) denotes the mass fraction of SF_6 in gas B (gas C) and A_1 (A_2) denotes the Atwood number of the first (second) initial interface.

The ambient pressure and temperature are 101.3 kPa and 295.5 ± 1.0 K, respectively. The IS with a Mach number of 1.20 ± 0.01 travels from left to right. The value of v_{IS} is $414 \pm 1\ \mathrm{m\,s^{-1}}$. The flow field is monitored by high-speed Schlieren photography. The frame rate of the high-speed video camera (FASTCAM SA5, Photron Limited) is 60 000 f.p.s. and the shutter time is 1 μs. The spatial resolution of the Schlieren images is $0.4\ \mathrm{mm\,pixel^{-1}}$. The flow field visualisation is limited within the range of $x \in [-50.0, 50.0]$ mm, as shown in figure 2(*b*).

4. Quasi-1-D experimental results and analysis

We shall first describe the reverberating waves observed from Schlieren images. Then, the interface displacements and velocities are measured and compared among different layer-thickness cases. Last, the speeds of the two interfaces after they are affected by the reverberating waves are deduced. In this way, a general 1-D theory for describing the interface motion is established.

4.1. *Experimental observation*

Schlieren images of the shock-induced quasi-1-D LMH fluid-layer evolution are shown in figure 3(*a–c*) for $2h_0 = 10.0$, 30.0 and 50.0 mm, respectively. The moment when the IS impacts the average position of the first initial interface (II_1) is defined as $t = 0$. Taking the L50-1D case as an example, the wave patterns and interface motions are discussed in detail. After the IS impacts the II_1, the reflected shock (RF_1) and the transmitted shock (TS_1) are immediately generated, and the shocked first interface (SI_1) begins to move forwards (46 μs). Then, the TS_1 impacts the second initial interface (II_2), and a transmitted shock (TS_2) is refracted outside the fluid layer and followed by the shocked second interface (SI_2) (262 μs). Meanwhile, a weak shock wave (RF_2) is reflected inside the fluid layer since the SI_2 is a fast/slow interface relative to the motion of the TS_1. Theoretically, after the RF_2 impacts the SI_1, rarefaction waves (RW) should be reflected inside the fluid layer since the SI_1 is a slow/fast interface relative to the motion of the RF_2. However, due to the RW's limited strength, the density variation induced by the RW is restricted, and it is challenging to distinguish the RW. Finally, all waves are refracted outside the fluid layer, and the interfaces at the two sides of the fluid layer move at the same speed. Moreover, it is noted that the two interfaces coalesce to one at a late time when the initial layer is very thin (1288 μs in the L10-1D case).

https://doi.org/10.1017/jfm.2022.213 Published online by Cambridge University Press

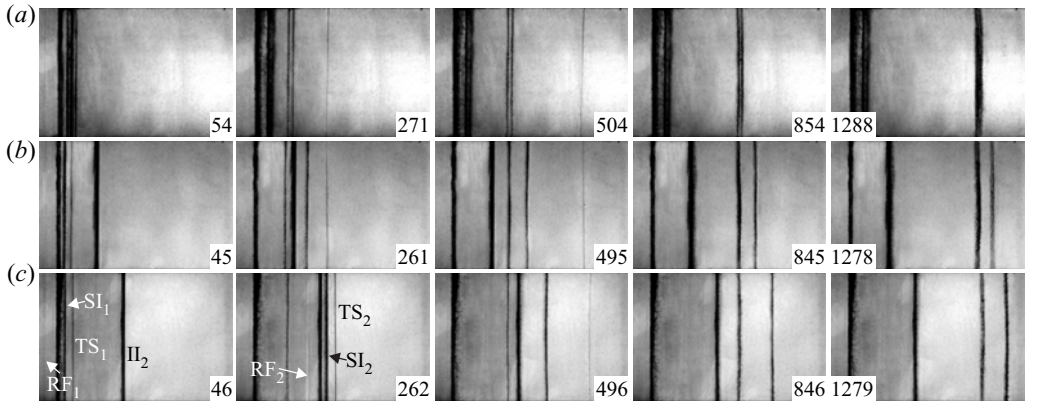


Figure 3. Schlieren images of the shock-induced quasi-1-D LMH fluid-layer evolution in cases (*a*) L10-1D, (*b*) L30-1D and (*c*) L50-1D, where SI_1 (SI_2) denotes the shocked first (second) interface, RF_1 (TS_1) denotes the reflected (transmitted) shock after the IS impacts II_1 and RF_2 (TS_2) denotes the reflected (transmitted) shock after the TS_1 impacts II_2. Numbers indicate time in μs.

The displacements (y_{SI_n}) and velocities (v_{SI_n}) of the two interfaces are measured from experiments ($n = 1$ for the first interface and 2 for the second interface), and are shown in figures 4(*a*) and 4(*b*), respectively. The pixel size of the Schlieren images introduces the experimental measurement uncertainty and is 0.4 mm in this work. The size of the error bars equals the size of the symbols in the figures. Time is scaled as $tv_{TS_1}/(2h_0)$, interface displacement is scaled as $(y_{SI_n} - y_{01})/(2h_0)$, with y_{01} denoting the initial position of the first interface, and interface velocity is scaled as $v_{SI_n}/\Delta v_1$. The values of v_{TS_1} and Δv_1 in all cases are calculated according to the 1-D gas dynamics theory (Drake 2018), as listed in table 2. The dimensionless displacements and velocities of the first (second) interface converge in all h_0 cases, as shown in figure 4(*a*,*b*), which indicates that the dimensionless movements of the two interfaces are independent of the initial layer thickness.

4.2. *Characteristics of reverberating waves*

The waves reverberating inside an LMH fluid layer are sketched in figure 5(*a–d*). To have a clear description of the interaction of a reverberating wave and interface, we first define several specific times including t_2^0 when the TS_1 impacts the II_2, t_1^* when the RF_2 impacts the SI_1 and t_2^* when the rarefaction wave head (RWH) impacts the SI_2. Then t_2^0, t_1^* and t_2^* can be evaluated as

$$\left.\begin{aligned} t_2^0 &= \frac{2h_0}{v_{TS_1}}, \\ t_1^* &= t_2^0 + \frac{2h_0 - t_2^0\Delta v_1}{\Delta v_1 - v_{RF_2}}, \\ t_2^* &= t_1^* + \frac{2h_0 - t_2^0\Delta v v_1 + (t_1^* - t_2^*)(\Delta v_2 - \Delta v_1)}{v_{RWH} - \Delta v_2}, \end{aligned}\right\} \tag{4.1}$$

in which v_{RF_2} represents the speed of the RF_2, v_{RWH} represents the speed of the RWH. The values of v_{RF_2}, v_{RWH} and Δv_2 are calculated according to the 1-D gas dynamics theory (Drake 2018), and then t_2^0, t_1^* and t_2^* are obtained, as listed in table 2.

https://doi.org/10.1017/jfm.2022.213 Published online by Cambridge University Press

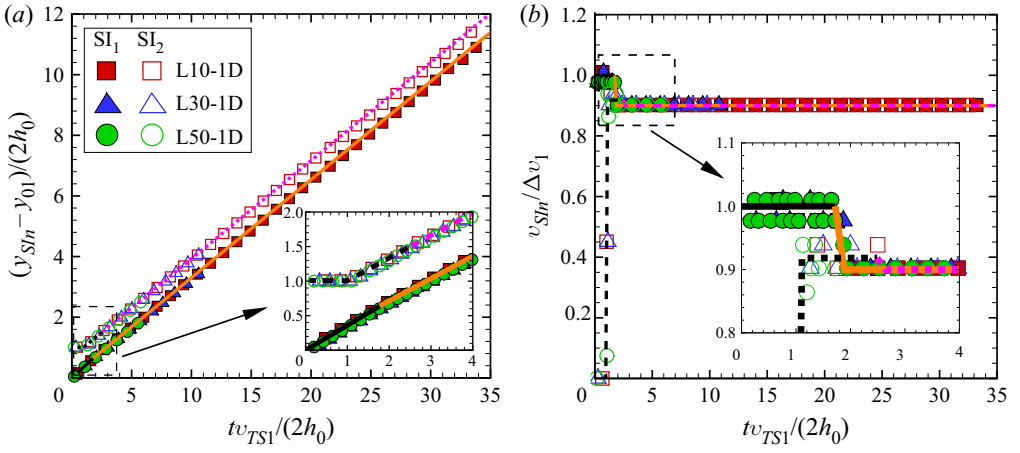


Figure 4. The dimensionless displacements (*a*) and velocities (*b*) of the first interface (solid symbols) and the second interface (hollow symbols). Black and orange solid lines represent the 1-D theory predictions for the first interface motions in Stages I ($t_1^* > t > 0$) and II ($t > t_1^*$), respectively. Black and purple dashed lines represent the 1-D theory predictions for the second interface motions in Stages I ($t_2^* > t > t_2^0$) and III ($t > t_2^+$), respectively.

Case	L10-1D	L30-1D	L50-1D	L10-IP	L10-AP	L30-IP	L30-AP	L50-IP	L50-AP
v_{t1}	222	222	222	229	222	236	236	244	236
v_{RF_2}	−104	−103	−104	−109	−104	−115	−115	−122	−116
v_{RWH}	254	254	253	260	253	266	268	277	267
v_{RWT}	252	253	252	258	252	264	266	275	265
Δv_1	79.8	79.8	79.9	81.1	79.8	82.5	82.5	84.1	82.6
Δv_2	73.3	73.6	72.8	72.9	72.8	72.7	74.4	75.2	72.8
v_1^*	71.9	72.3	71.3	71.3	71.3	70.8	72.9	73.6	70.8
v_2^+	72.0	72.4	71.4	71.4	71.4	70.9	73.0	73.7	70.9
v_{fn}	71.9	72.3	71.3	71.3	71.3	70.8	72.9	73.6	70.8
t_2^0	45	135	225	45	45	127	127	205	212
t_1^*	80	240	400	78	80	226	226	364	375
t_2^*	114	343	570	111	114	322	323	520	535

Table 2. Physical parameters of the waves and interfaces of an LMH fluid layer in the laboratory reference, where v_{TS_1} denotes the speed of the TS_1, v_{RF_2} denotes the speed of the RF_2, v_{RWH} denotes the speed of the RWH, v_{RWT} denotes the speed of the RWT, Δv_1 (Δv_2) denotes the speed of the SI_1 (SI_2) in Stage I, v_1^* denotes the speed of the SI_1 in Stage II, v_2^+ denotes the speed of the SI_2 in Stage III, v_{fn} denotes the asymptotic velocity of the two interfaces, t_2^0 denotes the specific time when the TS_2 impacts II_2, t_1^* denotes the specific time when the RF_2 impacts SI_1 and t_2^* denotes the specific time when the RWH impacts SI_2. RWT denotes the rarefaction wave tail. The units for speed and time are $m\,s^{-1}$ and μs, respectively.

After the RF_2 impacts the SI_1, the speed of the SI_1 decreases from Δv_1 to v_1^*. The values of v_1^* can be calculated according to the 1-D gas dynamics theory (Drake 2018), as listed in table 2. After the RW impact the SI_2, the speed of the SI_2 reduces from v_2^α to v_2^+. The interaction of the RW and a fast/slow interface (i.e. SI_2) is different from the interaction of the RW and a slow/fast interface previously investigated (Liang & Luo 2021*a*). Based on the 1-D gas dynamics theory (Velikovich & Phillips 1996; Drake 2018), v_2^+ can be

https://doi.org/10.1017/jfm.2022.213 Published online by Cambridge University Press

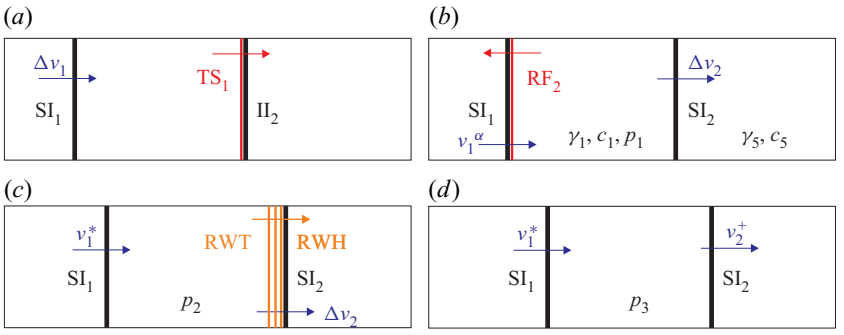


Figure 5. Sketches of (*a*) the interaction of the TS$_1$ and II$_2$ at t_2^0, (*b*) the interaction of the RF$_2$ and SI$_1$ at t_1^*, (*c*) the interaction of the RW and SI$_2$ at t_2^* and (*d*) the motions of the SI$_1$ and SI$_2$ when $t > t_2^+$.

calculated as

$$v_2^+ = \Delta v_2 + \frac{2c_5}{\gamma_5 - 1}[p_{31}^{(\gamma_5-1)/2\gamma_5} - 1], \tag{4.2}$$

where γ_5 is the specific heat ratio of gas C, c_5 is the sound speed of gas C after the TS$_1$ impacts the II$_2$. The only unknown parameter p_{31}, i.e. the ratio of the pressure of the flow after the RWT leaves the SI$_2$ (p_3) to the pressure of the flow between the RF$_2$ and SI$_2$ (p_1), as sketched in figure 5(*b*,*d*), satisfies

$$\frac{c_5}{c_1} = \frac{(\gamma_5 - 1)[p_{31}^{(\gamma_1-1)/2\gamma_1} - 2p_{21}^{(\gamma_1-1)/2\gamma_1} + 1]}{(\gamma_1 - 1)[1 - p_{31}^{(\gamma_5-1)/2\gamma_5}]}, \tag{4.3}$$

where γ_1 is the specific heat ratio of gas B, c_1 is the sound speed of gas B after the TS$_1$ impacts the II$_2$ and p_{21} is the ratio of the pressure of the flow between the RWT and SI$_1$ (p_2) to p_1. Then the v_2^+ can be calculated by solving (4.2)–(4.3), as listed in table 2.

The number of reverberating waves is infinite. However, the consecutive changes of pressure and velocity imparted by these reverberations decrease continuously, eventually converging to a well-defined asymptotic 1-D post-shock state. The influences of the reverberating waves on the 1-D and 2-D dynamics of the two interfaces should be considered (Aglitskiy *et al.* 2006) until the two interfaces enter the asymptotic post-shock state. A simple and advantageous method is adopted to judge whether the higher-order reverberations should be accounted for or not. The interaction of an IS with a semi-infinite interface separating two fluids with ρ_1 and ρ_3 is considered, and the intermediate layer is ignored. Then, the final post-shock velocity, v_{fn}, can be calculated according to the 1-D gas dynamics theory (Drake 2018). As listed in table 2, the asymptotic velocity v_{fn} is the same as v_1^* and is 0.1 % smaller than v_2^+. Therefore, it is reasonable to regard that, after the RWT leaves the SI$_2$, the motions of the two interfaces enter the asymptotic state. Unlike the sudden acceleration imposed by a shock wave on an interface, the interaction of the RW and an interface is generally regarded as a continuous process (Li & Book 1991; Li, Kailasanath & Book 1991; Morgan, Likhachev & Jacobs 2016; Morgan *et al.* 2018; Liang *et al.* 2020*b*; Liang & Luo 2021*a*). The length of the RW (L_{RW}), the interaction time of the RW with SI$_2$ (T_{RW}) and the average deceleration imposed on the SI$_2$ by the RW ($\bar{g}_{RW}$) are

https://doi.org/10.1017/jfm.2022.213 Published online by Cambridge University Press

Case	L10-1D	L30-1D	L50-1D	L10-IP	L10-AP	L30-IP	L30-AP	L50-IP	L50-AP
L_{RW}	0.05	0.15	0.28	0.06	0.06	0.20	0.16	0.27	0.33
T_{RW}	0.30	0.85	1.59	0.32	0.32	1.04	0.86	1.35	1.71
$\bar{g}_{RW}$	−4.88	−1.62	−0.98	−5.30	−4.89	−1.85	−1.84	−1.18	−1.12

Table 3. Physical parameters of the RW inside an LMH fluid layer. Here, L_{RW} denotes the length of the RW at t_2^*; T_{RW} denotes the interaction time of the RW and SI_2, and $\bar{g}_{RW}$ denotes the average deceleration imposed on the SI_2 by the RW. The units for length, time and deceleration are mm, μs and $10^6 \times \mathrm{m\,s^{-2}}$, respectively.

separately deduced as

$$\left.\begin{aligned} L_{RW} &= (v_{RWH} - v_{RWT})(t_2^* - t_1^*), \\ T_{RW} &= \frac{2L_{RW}}{2u_{RWT} - \Delta v_2 - v_2^+}, \\ \bar{g}_{RW} &= \frac{v_2^+ - \Delta v_2}{T_{RW}}, \end{aligned}\right\} \tag{4.4}$$

where u_{RWT} denotes the speed of the RWT. The values of L_{RW}, T_{RW} and $\bar{g}_{RW}$ in all cases are calculated according to (4.4), as listed in table 3. As the layer thickness increases, both the L_{RW} and T_{RW} increase, whereas the $|\bar{g}_{RW}|$ decreases.

It is evident that the motions of the two interfaces of a shocked LMH fluid layer can be divided into several stages, as illustrated in figure 4(*b*). Specifically, the first interface's motion can be separated into two stages: Stage I. Uniform motion with the Δv_1 during $t_1^* > t > 0$; Stage II. Uniform motion with the v_1^* during $t > t_1^*$. The second interface's motion can be divided into three stages: Stage I. Uniform motion with the Δv_2 during $t_2^* > t > t_2^0$; Stage II. Deceleration with the $\bar{g}_{RW}$ during $t_2^+ > t > t_2^*$ with $t_2^+ = t_2^* + T_{RW}$; Stage III. Uniform motion with the v_2^+ during $t > t_2^+$. In fact, the motions of the two interfaces can be described by the derived specific times (4.1) and interface velocities ((4.2)–(4.4)), which actually form a general 1-D theory for the interface motion. The predictions of the 1-D theory for the first interface motions in Stages I and II are marked with black and orange solid lines in figure 4(*a*,*b*), and they agree well with the experimental results. The predictions of the 1-D theory for the second interface motions in Stages I and III are marked as black and purple dashed lines, and they agree well with the experimental results. Due to the limited duration of Stage II for the second interface (e.g. T_{RW} is only around 1 μs in this study), the second interface motions in Stage II are not represented in figure 4(*a*,*b*).

5. Quasi-2-D experimental results and analysis

We shall first describe the deformations of the two interfaces observed from Schlieren images. Then, the amplitude growth rates are acquired from experiments and compared with the predictions of the LL model. Later, the interface-coupling effect on the RMI of the two interfaces is quantified and discussed. Last, the influences of the reverberating waves and the nonlinearity on the hydrodynamic instabilities of the two interfaces are modelled.

https://doi.org/10.1017/jfm.2022.213 Published online by Cambridge University Press

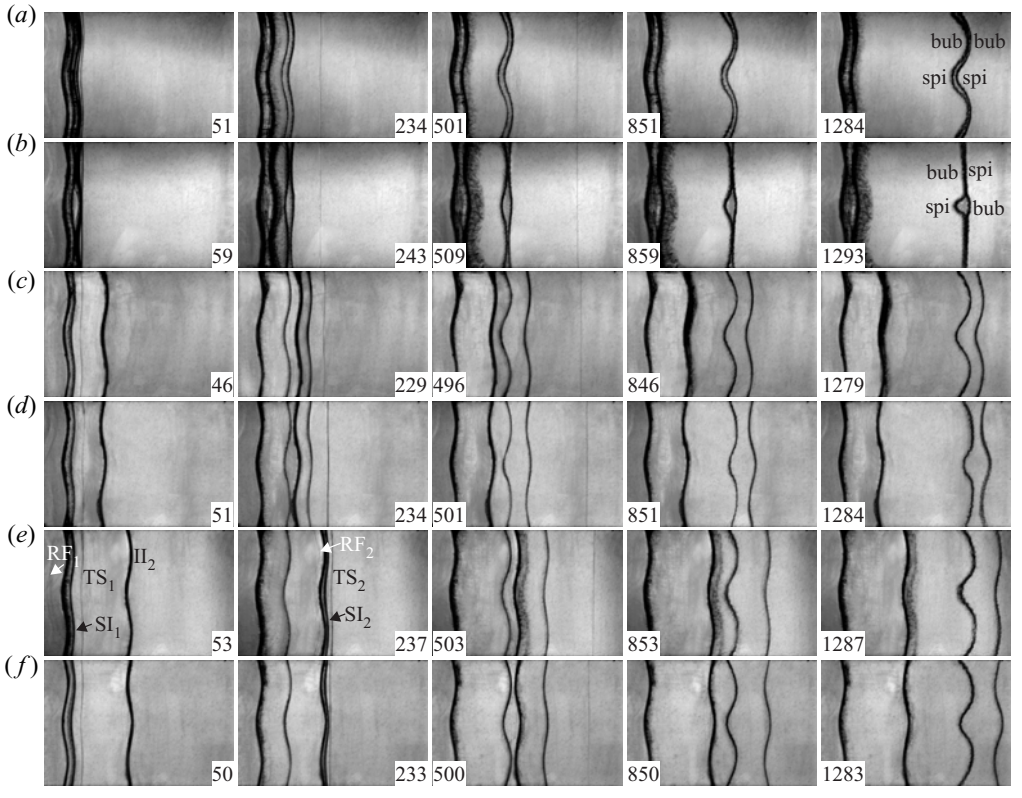


Figure 6. Schlieren images of the shock-induced quasi-2-D LMH fluid-layer evolution in cases (*a*) L10-IP, (*b*) L10-AP, (*c*) L30-IP, (*d*) L30-AP, (*e*) L50-IP and (*f*) L50-AP. Here, 'bub' and 'spi' denote bubble and spike, respectively. Numbers denote time in μs.

5.1. *Experimental results*

Schlieren images of the shock-induced quasi-2-D LMH fluid-layer evolution are shown in figure 6(*a–f*). Taking the L50-IP case as an example, the deformations of the two interfaces are discussed in detail. After the IS impacts the perturbed II_1, the rippled RF_1 is reflected outside the fluid layer, and the rippled TS_1 moves towards the II_2 (53 μs). Meanwhile, the perturbation on the SI_1 increases due to the vorticity deposited by the IS on the SI_1. After the TS_1 impacts the perturbed II_2, the rippled TS_2 is refracted outside the fluid layer, and the rippled RF_2 is reflected inside the fluid layer. Meanwhile, the perturbation on the SI_2 increases due to the vorticity deposited by the TS_1 on the SI_2 (237 μs). Finally, all waves are refracted outside the fluid layer, and the two interfaces evolve with the same phase as their initial perturbations. In addition, different from the large h_0 cases, portions of the two interfaces collide when h_0 is limited. For example, bubbles of the two interfaces collide at 1284 μs in the L10-IP case, and the bubble of the SI_1 collides with the spike of the SI_2 at 509 μs in the L10-AP case.

The experimental amplitude growth rate of the first interface ($\dot{a}_1^{exp}$) and that of the second interface ($\dot{a}_2^{exp}$) in Stage I are acquired by linearly fitting the experimental data, as listed in table 4. In the three in-phase cases, as h_0 decreases, both v_1^{exp} and $\dot{a}_2^{exp}$ increase. However, in the three anti-phase cases, as h_0 decreases, both $\dot{a}_1^{exp}$ and $|\dot{a}_2^{exp}|$ decrease. The results indicate that the RMI of an LMH fluid layer is influenced by the initial layer

https://doi.org/10.1017/jfm.2022.213 Published online by Cambridge University Press

Case	L10-IP	L10-AP	L30-IP	L30-AP	L50-IP	L50-AP
$\dot{a}_1^{exp}$	7.8 ± 0.6	4.5 ± 0.4	6.9 ± 0.4	6.1 ± 0.4	6.5 ± 0.4	6.5 ± 0.4
$\dot{a}_2^{exp}$	4.5 ± 0.4	0.4 ± 0.2	3.1 ± 0.2	-1.8 ± 0.2	2.6 ± 0.2	-2.6 ± 0.2
$\dot{a}_1^l$	8.2	4.9	7.3	6.2	6.6	6.5
$\dot{a}_2^l$	4.9	0.4	3.3	−1.7	2.7	−2.6
ψ_1	1.19	0.69	1.09	0.93	1.03	0.97
ψ_2	2.13	−0.20	1.22	0.74	1.08	0.96
$\dot{a}_1^*$	7.2	4.1	5.5	4.8	4.7	4.2
$\dot{a}_2^+$	4.7	0.1	3.1	−1.5	2.5	−2.3

Table 4. The linear amplitude growth rates of the two interfaces of an LMH fluid layer, where $\dot{a}_1^{exp}$ ($\dot{a}_2^{exp}$) denotes the experimental amplitude growth rate of the first (second) interface in Stage I, $\dot{a}_1^l$ ($\dot{a}_2^l$) denotes the amplitude growth rate of the first (second) interface in Stage I calculated with (2.14) (2.15); ψ_1 (ψ_2) quantifies the interface-coupling effect on the RMI of the first (second) interface calculated with (5.1); $\dot{a}_1^*$ denotes the amplitude growth rate of the first interface at t_1^* calculated with (5.2) and $\dot{a}_2^+$ denotes the amplitude growth rate of the second interface at t_2^+ calculated with (5.4)–(5.6).

thickness and phases of the two interfaces, i.e. the interface-coupling effect. Due to the interface-coupling effect on the RMI of the second interface in the L10-AP case, an opposite sign of the amplitude growth rate of a fast/slow interface to its initial perturbation amplitude is observed. For a semi-infinite fast/slow Richtmyer–Meshkov (RM) unstable interface, the sign of its amplitude growth rate should be the same as the sign of its initial amplitude (Richtmyer 1960). In general, the amplitude growth rate of a semi-infinite slow/fast RM unstable interface has the opposite sign to its initial amplitude, which is ascribed to the phase reversal (Brouillette 2002). The phase reversal of a shocked fast/slow interface (the second interface in the L10-AP case) is called 'abnormal phase reversal' in this study.

The values of $\dot{a}_1^l$ and $\dot{a}_2^l$ are calculated with the LL model and listed in table 4, and a good agreement with the experimental results is found. It is noted that $\dot{a}_2^l$ also has the opposite sign to $a_2(0)$ in the L10-AP case.

5.2. *The interface-coupling effect*

To quantify the interface-coupling effect on the RMI of an arbitrary fluid layer, we first propose a normalised growth rate (ψ_n) which is defined as the ratio of the amplitude growth rate of the nth interface calculated with the LL model to that calculated with the impulsive theory (Richtmyer 1960),

$$\left.\begin{aligned} \psi_1 &= \frac{(R_1+1)(2R_3\xi+\xi^2+1)-(R_1+1)(R_3-1)(1-\xi^2)/[\epsilon(R_1-1)]}{2\xi(R_1R_3+1)+(R_1+R_3)(\xi^2+1)}, \\ \psi_2 &= \frac{\epsilon(R_1-1)(R_3+1)(\xi^2-1)/(R_3-1)+(R_3+1)(2R_1\xi+\xi^2+1)}{2\xi(R_1R_3+1)+(R_1+R_3)(\xi^2+1)}. \end{aligned}\right\} \tag{5.1}$$

The values of ψ_1 and ψ_2 in all the LMH layer cases are listed in table 4. It is found that $\psi_1 > 1$ and $\psi_2 > 1$ in the three in-phase cases, and $\psi_1 < 1$ and $|\psi_2| < 1$ in the three anti-phase cases, indicating that the interface-coupling effect leads to the two in-phase interfaces being more unstable than the semi-infinite RMI, and the two anti-phase interfaces being more stable than the semi-infinite RMI, under the LMH fluid-layer

https://doi.org/10.1017/jfm.2022.213 Published online by Cambridge University Press

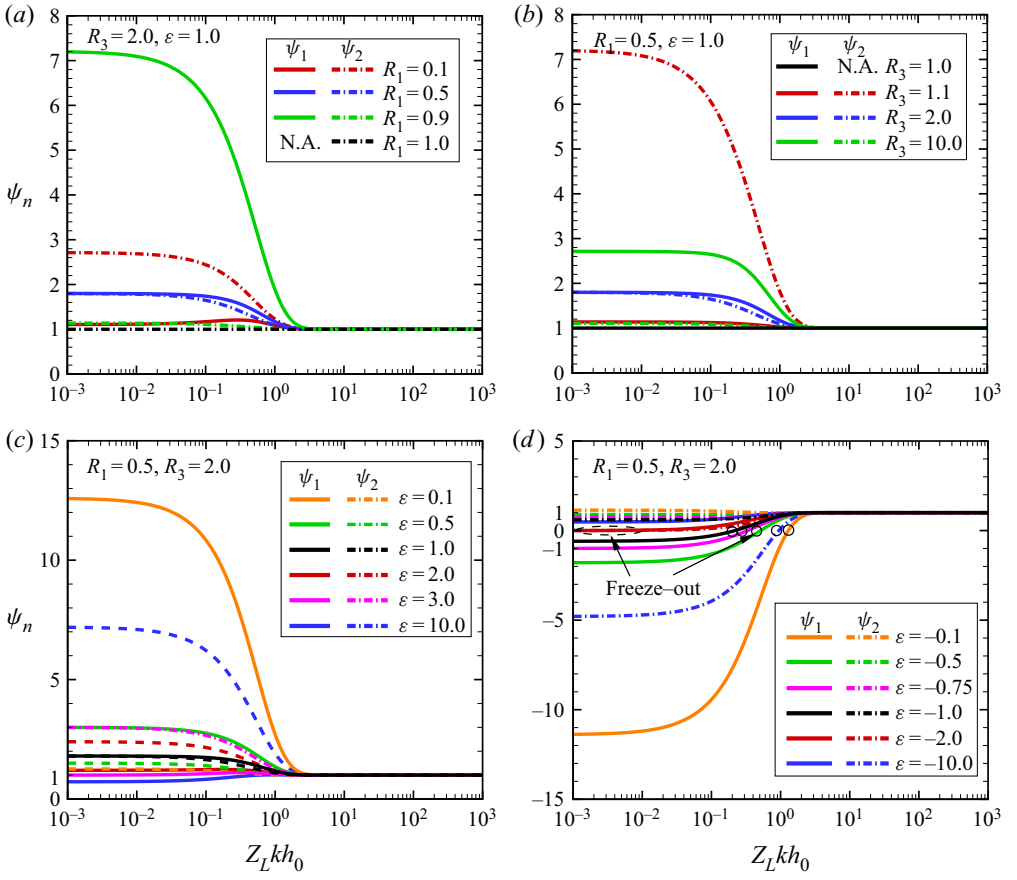


Figure 7. Value of ψ_n of the nth interface vs $Z_L k h_0$ under (a) different R_1 conditions, (b) different R_3 conditions, (c) different ϵ (> 0) conditions and (d) different ϵ (< 0) conditions. Hollow circles represent the instability freeze out of the first or second interface.

condition. The conclusion is opposite to the A/B/A-type fluid-layer counterpart, i.e. the interface-coupling effect results in the two in-phase interfaces of an A/B/A-type fluid layer being more stable, and the two anti-phase interfaces being more unstable (Liang & Luo 2021*a*, 2022).

It is proved that the interface-coupling effect is determined by the density ratios of the fluids outside the layer to the fluid inside the layer (R_1 and R_3), the post-shock amplitude ratio of the two interfaces (ϵ) and the dimensionless post-shock layer thickness ($Z_L k h_0$). The values of ψ_n of an LMH fluid layer vs $Z_L k h_0$ under different R_1, R_3 and ϵ conditions are calculated based on (5.1), as shown in figure 7(*a–d*), respectively.

In figure 7(*a*), we plot ψ_1 and ψ_2 as functions of $Z_L k h_0$ for the case R_1 varying from 0.1 to 1.0, $R_3 = 2.0$ and $\epsilon = 1.0$. When $Z_L k h_0 < 2$, $\psi_1 > 1$ and $\psi_2 > 1$ indicate that the interface-coupling effect results in the two interfaces of an LMH fluid layer being more unstable if the two interfaces are initially in phase. Specifically, when $R_1 \leq (1/R_3)$ ($R_1 > (1/R_3)$), $\psi_1 \leq \psi_2$ ($\psi_1 > \psi_2$), indicating the interface-coupling effect destabilises the second interface more (less) than the first interface. When $Z_L k h_0 > 2$, ψ_1 and ψ_2 converge at 1, revealing that the interface-coupling effect has a negligible influence on the RMI of a fluid layer.

https://doi.org/10.1017/jfm.2022.213 Published online by Cambridge University Press

In figure 7(*b*), we plot ψ_1 and ψ_2 as functions of $Z_L kh_0$ for the case R_3 varying from 1.0 to 10.0, $R_1 = 0.5$ and $\epsilon = 1.0$. It is found that, when $R_3 \leq (1/R_1)$ $(R_3 > (1/R_1))$, $\psi_1 \leq \psi_2$ $(\psi_1 > \psi_2)$, indicating the interface-coupling effect destabilises the second interface more (less) than the first interface, which agrees well with the findings in figure 7(*a*).

In figure 7(*c*), we plot ψ_1 and ψ_2 as functions of $Z_L kh_0$ for the case ϵ varying from 0.1 to 10.0, $R_1 = 0.5$ and $R_3 = 2.0$. It is found that when $3.0 > \epsilon > 0$, $\psi_1 > 1$ and $\psi_2 > 1$, indicating that the interface-coupling effect results in both interfaces being more unstable. Specifically, the interface-coupling effect promotes the RMI of the first interface more than the second interface counterpart (i.e. $\psi_1 > \psi_2$) when $1.0 > \epsilon > 0$, and the interface-coupling effect promotes the RMI of the second interface more than the first interface counterpart (i.e. $\psi_1 < \psi_2$) when $3.0 > \epsilon > 1.0$. In addition, when $\epsilon > 3.0$, $\psi_1 < 1$ and $\psi_2 > 1$, demonstrating that the interface-coupling effect leads to the first interface being more stable, and the second interface being more unstable. Overall, the two in-phase interfaces of an LMH fluid layer are generally destabilised by the interface-coupling effect, but the first interface might be stabilised if the ϵ is large.

In figure 7(*d*), we plot ψ_1 and ψ_2 as functions of $Z_L kh_0$ for the case ϵ varying from -0.1 to -10.0, $R_1 = 0.5$ and $R_3 = 2.0$. It is found that, when $0 > \epsilon > -2.0$ and $Z_L kh_0 < 2$, $\psi_1 < 0$ and $\psi_2 > 0$, indicating that the interface-coupling effect results in the abnormal phase reversal of the first interface. The interface-coupling effect leads to the first interface being more unstable when $0 > \epsilon > -0.75$ and the second interface being more stable when $0 > \epsilon > -0.5$. When $\epsilon < -2.0$, $1 > \psi_1 > 0$ and $\psi_2 < 0$, demonstrating that the interface-coupling effect causes the first interface to be more stable, and abnormal phase reversal of the second interface. Moreover, the instability freeze out of the first interface or the second interface occurs when $\psi_1 = 0$ or $\psi_2 = 0$, as marked with hollow circles in figure 7(*d*).

In summary, (i) when $Z_L kh_0 < 2$, the interface-coupling effect has a non-negligible influence on the RMI of a fluid layer; (ii) the interface-coupling effect destabilises (stabilises) the nth interface when $|\psi_n| > 1$ $(|\psi_n| < 1)$; (iii) the two in-phase interfaces of an LMH fluid layer are generally destabilised by the interface-coupling effect, but the first interface might be stabilised if ϵ is large; (iv) the instability freeze out and the abnormal phase reversal of the nth interface occurs when $\psi_n = 0$ and $\psi_n < 0$, respectively.

5.3. *Effect of reverberating waves*

As stated in the 1-D cases, there exist reverberating waves inside the layer which in turn will interact with the two interfaces. In the 2-D cases, reverberating waves will impose additional vorticity and/or accelerations on the interface in its Stage II.

In Stage II for the first interface, the RF_2 impulsively impacts the SI_1 and deposits the additional vorticity on the first interface, causing the post-shock amplitude growth rate of the first interface, i.e. $\dot{a}_1^*$, to be different from $\dot{a}_1^l$. Because of the baroclinic mechanism created by the misalignment of the density gradient $(\nabla\rho)$ and the pressure gradient (∇p), the RF_2 deposits vorticity with an opposite direction to the vorticity deposited by the IS on the first interface, as sketched in figure 8(*a*). Therefore the RF_2 imposes an additional RMI on the first interface and leads to the first interface being more stable. Since the first interface evolves in the linear regime before the RF_2 impacts it, it is reasonable to adopt the re-shock impulsive theory proposed by Mikaelian (1985) to modify the LL model and

https://doi.org/10.1017/jfm.2022.213 Published online by Cambridge University Press

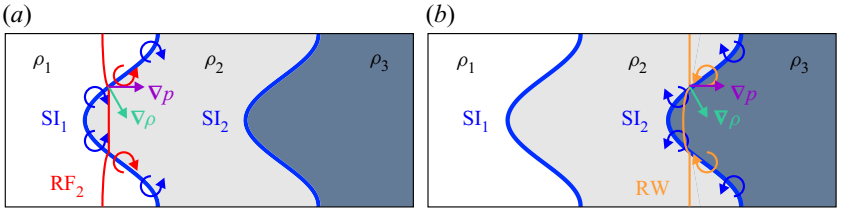


Figure 8. Sketches of the interaction of the RF$_2$ and SI$_1$ (*a*) and the interaction of the RW and SI$_2$ (*b*). The blue (red) arc with an arrow in (*a*) illustrates the vorticity deposition induced by the IS (RF$_2$) on the first interface. The blue (orange) arc with an arrow in (*b*) represents the vorticity deposition induced by the TS$_1$ (RW) on the second interface. The purple (green) arrows represent the pressure (density) gradient ∇p ($\nabla \rho$).

calculate a_1^* as

$$\dot{a}_1^* = \dot{a}_1^l + k a_1^* A_1 (v_1^* - \Delta v_1), \tag{5.2}$$

with a_1^* denoting the first interface amplitude at t_1^*

$$a_1^* = Z_1 a_1(0) + \dot{a}_1^l t_1^*. \tag{5.3}$$

The values of $\dot{a}_1^*$ in all cases are listed in table 4.

In Stage II for the second interface, the RW continuously deposit additional vorticity on the second interface, causing the post-rarefaction amplitude growth rate of the second interface, i.e. $\dot{a}_2^+$, to be different from $\dot{a}_2^l$. The RW induce vorticity deposition with the opposite direction to the vorticity deposited by the TS$_1$ on the second interface, as sketched in figure 8(*b*). Therefore, the RW impose RTS on the second interface, leading to the second interface being more stable. Here, we adopt the potential flow model proposed by Zhang & Guo (2016) considering the universal curves of all spikes and bubbles at any density ratio, to quantify the RTS imposed by the RW on the second interface and modify the LL model. The expressions for the second interface bubble/spike amplitude growth rate ($\dot{a}_{2b/2s}^*$) in Stage II are

$$\ddot{a}_{2b/2s}^* = \alpha_{b/s} k [(\dot{a}_{2b/2s}^*)^2 - (\dot{a}_{2b/2s}^{qs})^2], \tag{5.4}$$

with

$$\dot{a}_{2b/2s}^{qs} = \sqrt{\frac{A_2 |\bar{g}_{RW}|}{3k} \frac{8}{(1 \pm A_2)(3 \pm A_2)} \frac{\left[3 \pm A_2 + \sqrt{2(1 \pm A_2)}\right]^2}{\left[4(3 \pm A_2) + \sqrt{2(1 \pm A_2)}(9 \pm A_2)\right]}}, \tag{5.5}$$

and

$$\alpha_{b/s} = \frac{3}{4} \frac{(1 \pm A_2)(3 \pm A_2)}{\left[3 \pm A_2 + \sqrt{2(1 \pm A_2)}\right]} \frac{\left[4(3 \pm A_2) + \sqrt{2(1 \pm A_2)}(9 \pm A_2)\right]}{\left[\sqrt{3 \pm A_2} + 2\sqrt{2(1 \pm A_2)}(3 \mp A_2)\right]}. \tag{5.6}$$

The upper (lower) sign of $\pm$ and $\mp$ applies to the bubble (spike). Note that the interface-coupling effect is considered since the initial $\dot{a}_{2b/2s}^*$ equals $\dot{a}_2^l$ at t_2^*. The average values of $\dot{a}_{2b}^*$ and $\dot{a}_{2s}^*$ at t_2^+, i.e. $\dot{a}_2^+$, in all cases are calculated based on (5.4)–(5.6), as listed in table 4. The value of $\dot{a}_2^+$ is only 0.1 m s^{-1} in the L10-AP case, which indicates that the second interface's instability is close to being frozen due to both the interface-coupling effect and the RTS induced by the RW. In summary, the reverberating waves inside an LMH fluid layer, including the RF$_2$ and RW, stabilise the two interfaces.

https://doi.org/10.1017/jfm.2022.213 Published online by Cambridge University Press

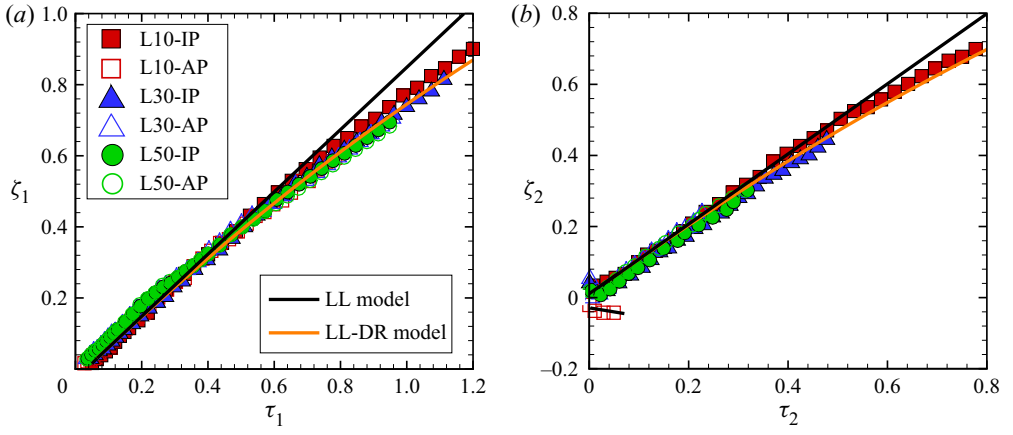


Figure 9. Comparisons of the dimensionless amplitudes of the first interface (*a*), and the second interface (*b*). Black and orange lines represent the theoretical predictions for the two interface amplitudes based on the LL model and the LL-DR model, respectively.

5.4. *Nonlinear model for a shocked LMH fluid layer*

The time-varying amplitudes of the two interfaces are measured and are shown in figures 9(*a*) and 9(*b*). These clearly show a nonlinear behaviour after a certain time. For the first interface, time is scaled as $\tau_1 = k\dot{a}_1^l t$, and amplitude is scaled as $\zeta_1 = k(a_1 - Z_1 a_1(0))$. For the second interface, time is scaled as $\tau_2 = k|\dot{a}_2^l|(t - t_2^0)$ and amplitude is scaled as $\zeta_2 = k(|a_2| - |Z_2 a_2(0)|)$. The dimensionless a_1 converges in all cases, indicating that the initial layer-thickness and amplitude combination has limited influence on the nonlinear behaviour of the first interface perturbation growth. The dimensionless a_2 converges in all cases except for the L10-AP case (due to the abnormal phase reversal of the second interface in the L10-AP case). The LL model's predictions for a_1 and a_2 by considering the interface-coupling effect and the additional instabilities induced by the reverberating waves are shown with black lines in figure 9(*a*,*b*), and they agree well with all the experimental results before dimensionless time 0.4. Due to the nonlinearity effect on the RMI (Velikovich & Dimonte 1996; Zhang & Sohn 1997; Nishihara *et al.* 2010), a_1 and a_2 deviate from the LL model's predictions after dimensionless time 0.4. Therefore, the nonlinearity effect on the RMI of an LMH fluid layer should be considered in Stage II for the first interface and in Stage III for the second interface.

The nonlinearity of single-mode RMI generally can be interpreted by the perturbation expansion model (Zhang & Sohn 1997; Vandenboomgaerde, Gauthier & Mügler 2002), the vortex model (Jacobs & Sheeley 1996; Peng *et al.* 2021), the potential flow model (Hecht, Alon & Shvarts 1994; Mikaelian 1998, 2003; Sadot *et al.* 1998; Zhang 1998; Goncharov 2002; Sohn 2003; Dimonte & Ramaprabhu 2010; Zhang & Guo 2016; Zhang, Deng & Guo 2018), etc. First, the perturbation expansion model (Zhang & Sohn 1997; Vandenboomgaerde *et al.* 2002) is applicable for quantifying the development of high-order harmonics and describing the interface deformation in the weakly nonlinear regime. Since the effective time scope of the perturbation expansion model is short, we do not utilise such a model to quantify the nonlinearity of RMI. Second, the vortex model (Jacobs & Sheeley 1996; Peng *et al.* 2021) was derived with the assumption that the 'mushroom' structure on the spike is the manifestation of the vortex core induced by the initial thin vortex sheet on the interface. In other words, there should be enough time for

https://doi.org/10.1017/jfm.2022.213 Published online by Cambridge University Press

the vortex on the interface to merge into point vortices. The vortex model is applicable for the RMI in the late nonlinear regime and, therefore, we do not adopt such a model to quantify the nonlinearity of the RMI. Third, most potential flow models (Hecht *et al.* 1994; Mikaelian 1998, 2003; Zhang 1998; Goncharov 2002; Sohn 2003) established two decades ago are suitable for quantifying the asymptotic growth trend of the nonlinear RMI. The potential flow model deduced by Sadot *et al.* (1998) is the pioneering one covering both the linear growth rate and the nonlinearity of the RMI. However, tuning parameters C and E are adopted in such a model to match experimental results, and their exact values at intermediate Atwood numbers remain uncertain (Mansoor *et al.* 2020). The potential flow models recently proposed by Zhang & Guo (2016) and Zhang *et al.* (2018) have attracted much attention and have been validated by several independent experiments and simulations. Nevertheless, such potential flow models are available when the initial amplitude–wavelength ratio is small (< 0.04).

The potential flow model proposed by Dimonte & Ramaprabhu (2010), i.e. the DR model, considering various amplitude–wavelength ratios and density ratios, has been adopted to successfully quantify the nonlinearity of RMI of SF_6 gas layers (Liang & Luo 2021*a*) and helium gas layers (Liang & Luo 2022). Here, we extend the LL model to a nonlinear one by combining it with the DR model to describe the nonlinearity of RMI. The expressions of the combined model (i.e. LL–DR model) for the first interface bubble/spike amplitude growth rate ($\dot{a}^{nl}_{1b/1s}$) and the second interface bubble/spike amplitude growth rate ($\dot{a}^{nl}_{2b/2s}$) are

$$\left.\begin{aligned} \dot{a}^{nl}_{1b/1s} &= \frac{\dot{a}^{*}_{1}\left[1+(1\mp A_1)k\dot{a}^{*}_{1}t\right]}{1+C_{1b/1s}k\dot{a}^{*}_{1}t+(1\mp A_1)F_{1b/1s}(k\dot{a}^{*}_{1}t)^2}, \\ \dot{a}^{nl}_{2b/2s} &= \frac{\dot{a}^{+}_{2}\left[1+(1\mp A_2)k|\dot{a}^{+}_{2}|t\right]}{1+C_{2b/2s}k|\dot{a}^{+}_{2}|t+(1\mp A_2)F_{2b/2s}(k|\dot{a}^{+}_{2}|t)^2}, \end{aligned}\right\} \tag{5.7}$$

with

$$\left.\begin{aligned} C_{1b/1s} &= \frac{4.5\pm A_1+(2\mp A_1)kZ_1a_1(0)}{4}, \\ C_{2b/2s} &= \frac{4.5\pm A_2+(2\mp A_2)k|Z_2a_2(0)|}{4}, \end{aligned}\right\} \tag{5.8}$$

and

$$F_{1b/1s}=1\pm A_1, \quad F_{2b/2s}=1\pm A_2. \tag{5.9a,b}$$

The upper (lower) sign of $\pm$ and $\mp$ in (5.7)–(5.9a,b) applies to the bubble (spike). The LL–DR model predictions for a_1 and a_2 are shown with orange lines in figures 9(a) and 9(b), respectively, and they agree well with the experimental results.

6. Conclusions

A fluid layer with a LMH gas configuration is experimentally and theoretically considered. This kind of LMH fluid layer is of A/B/C-type and has two consecutive fast/slow interfaces. A linear stability analysis is first performed to derive the LL model to quantify the RMI on the two interfaces of an arbitrary fluid layer in the weak-shock limit. Shock-tube experiments are performed to investigate the wave patterns, interface motions and hydrodynamic instabilities of the two interfaces of an LMH fluid layer. The soap film technique is extended to create three quasi-1-D fluid-layers with different layer thicknesses

https://doi.org/10.1017/jfm.2022.213 Published online by Cambridge University Press

and six quasi-2-D fluid layers with diverse layer-thickness and amplitude combinations. Schlieren photography combined with a high-speed camera provides legible experimental pictures. The shock/RW reverberating inside the layer are focused. The hydrodynamic instabilities of a shocked LMH fluid layer are well quantified with the models adopted in this study.

First, the wave patterns and interface motions in the three quasi-1-D LMH fluid layer cases are studied. The shock wave reflected from the second interface impulsively decelerates the first interface, and the RW reflected from the first interface continuously decelerate the second interface. The motions of the two interfaces finally enter the asymptotic state. It is observed that the two interfaces collide when the initial fluid layer is very thin. A general 1-D theory is adopted to describe the motions of the two interfaces.

Second, the hydrodynamic instabilities of a shocked quasi-2-D LMH fluid layer are investigated. The final phases of the two interfaces are the same as the two interfaces' initial perturbations. On comparing with the semi-infinite single-mode RMI, the interface-coupling effect destabilises the two initial in-phase interfaces but stabilises the two initial anti-phase interfaces of an LMH fluid layer in the experiments. The interface-coupling effect leads to the abnormal phase reversal of the second when the initial LMH fluid layer is very thin, and the two interfaces are anti-phase. The shock reflected from the second interface induces the additional RMI of the first interface, resulting in the first interface being more stable. The RW reflected from the first interface impose the additional RTS of the second interface, resulting in the second interface being more stable. Moreover, the nonlinearity effect on the RMI of the two interfaces is non-negligible after dimensionless time 0.4. The nonlinearity of the RMI of an LMH fluid layer is independent of the layer-thickness and amplitude combinations.

Third, the LL model is validated by the present experiments. It is proved that the interface-coupling effect is decided by the density ratios of the gases outside the fluid layer to the gas inside the fluid layer, the post-shock amplitude ratio of the two interfaces and the dimensionless post-shock layer thickness. Four findings are noteworthy: (i) when $Z_L k h_0 < 2$, the interface-coupling effect has a non-negligible influence on the RMI of a fluid layer; (ii) the interface-coupling effect destabilises (stabilises) the nth interface when $|\psi_n| > 1$ ($|\psi_n| < 1$); (iii) the two in-phase interfaces of an LMH fluid layer are generally destabilised by the interface-coupling effect, but the first interface might be stabilised if ϵ is large; (iv) the instability freeze out and the abnormal phase reversal of the nth interface occurs when $\psi_n = 0$ and $\psi_n < 0$, respectively. Furthermore, the additional RMI induced by the reflected shock on the first interface can be well described by the re-shock impulsive theory (Mikaelian 1985), and the additional RTS imposed by the RW on the second interface can be well described with the modified potential flow model (Zhang & Guo 2016). Finally, the LL model is combined with the potential flow model (Dimonte & Ramaprabhu 2010) to quantify the late-time nonlinear amplitude growths of the two interfaces.

Our findings indicate that we may manipulate the reverberating waves and the interface coupling in an LMH fluid layer to suppress the hydrodynamic instabilities, which may be useful for ICF capsule design. It is worth looking forward to testing the established models in this study with the experiments on the shock-induced heavy/medium/light fluid-layer evolution in the near future. Moreover, although the amplitude growths of the two interfaces are reported in this study, the mixed mass and normalised mixed mass are important quantities for evaluating the mixing and are key parameters in ICF applications

https://doi.org/10.1017/jfm.2022.213 Published online by Cambridge University Press

(Zhou, Cabot & Thornber 2016). We look forward to combing the soap film technique with a high-speed planar laser-induced fluorescence system to obtain the mixed mass and normalised mixed mass of a shocked fluid layer soon.

Acknowledgements. The authors appreciate the valuable suggestions of the reviewers. The authors are grateful for the help of Dr L. Liu in performing experiments.

Funding. This work was supported by the Natural Science Foundation of China (Nos. 91952205 and 11625211) and Tamkeen under the NYU Abu Dhabi Research Institute grant CG002.

Declaration of interests. The authors report no conflict of interest.

Author ORCIDs.
Yu Liang https://orcid.org/0000-0002-3254-7073;
Xisheng Luo https://orcid.org/0000-0002-4303-8290.

References

Aglitskiy, Y., *et al.* 2006 Perturbation evolution started by Richtmyer–Meshkov instability in planar laser targets. *Phys. Plasmas* **13** (8), 080703.

Balakumar, B.J., Orlicz, G.C., Ristorcelli, J.R., Balasubramanian, S., Prestridge, K.P. & Tomkins, C.D. 2012 Turbulent mixing in a Richtmyer–Meshkov fluid layer after reshock: velocity and density statistics. *J. Fluid Mech.* **696**, 67–93.

Balakumar, B.J., Orlicz, G.C., Tomkins, C.D. & Prestridge, K. 2008 Simultaneous particle-image velocimetry-planar laser-induced fluorescence measurements of Richtmyer–Meshkov instability growth in a gas curtain with and without reshock. *Phys. Fluids* **20**, 124103.

Brouillette, M. 2002 The Richtmyer–Meshkov instability. *Annu. Rev. Fluid Mech.* **34**, 445–468.

Budzinski, J.M., Benjamin, R.F. & Jacobs, J.W. 1994 Influence of initial conditions on the flow patterns of a shock-accelerated thin fluid layer. *Phys. Fluids* **6**, 3510–3512.

Dimonte, G. & Ramaprabhu, P. 2010 Simulations and model of the nonlinear Richtmyer–Meshkov instability. *Phys. Fluids* **22**, 014104.

Ding, J., Li, J., Sun, R., Zhai, Z. & Luo, X. 2019 Convergent Richtmyer–Meshkov instability of a heavy gas layer with perturbed outer interface. *J. Fluid Mech.* **878**, 277–291.

Drake, R.P. 2018 *High-Energy-Density Physics: Foundation of Inertial Fusion and Experimental Astrophysics*. Springer.

Fraley, G. 1986 Rayleigh–Taylor stability for a normal shock wave-density discontinuity interaction. *Phys. Fluids* **29**, 376–386.

Goncharov, V.N. 2002 Analytical model of nonlinear, single-mode, classical Rayleigh–Taylor instability at arbitrary Atwood numbers. *Phys. Rev. Lett.* **88**, 134502.

Haines, B.M., *et al.* 2021 Constraining computational modeling of indirect drive double shell capsule implosions using experiments. *Phys. Plasmas* **28** (3), 032709.

Hecht, J., Alon, U. & Shvarts, D. 1994 Potential flow models of Rayleigh–Taylor and Richtmyer–Meshkov bubble fronts. *Phys. Fluids* **6**, 4019–4030.

Jacobs, J.W., Jenkins, D.G., Klein, D.L. & Benjamin, R.F. 1995 Nonlinear growth of the shock-accelerated instability of a thin fluid layer. *J. Fluid Mech.* **295**, 23–42.

Jacobs, J.W., Klein, D.L., Jenkins, D.G. & Benjamin, R.F. 1993 Instability growth patterns of a shock-accelerated thin fluid layer. *Phys. Rev. Lett.* **70**, 583–586.

Jacobs, J.W. & Sheeley, J.M. 1996 Experimental study of incompressible Richtmyer–Meshkov instability. *Phys. Fluids* **8**, 405–415.

Kuranz, C.C., *et al.* 2018 How high energy fluxes may affect Rayleigh–Taylor instability growth in young supernova remnants. *Nat. Commun.* **9**, 1564.

Li, C. & Book, D.L. 1991 Instability generated by acceleration due to rarefaction waves. *Phys. Rev.* A **43** (6), 3153.

Li, J., Ding, J., Si, T. & Luo, X. 2020 Convergent Richtmyer–Meshkov instability of light gas layer with perturbed outer surface. *J. Fluid Mech.* **884**, R2.

Li, C., Kailasanath, K. & Book, D.L. 1991 Mixing enhancement by expansion waves in supersonic flows of different densities. *Phys. Fluids* A **3** (5), 1369–1373.

Liang, Y., Liu, L., Zhai, Z., Ding, J., Si, T. & Luo, X. 2021 Richtmyer–Meshkov instability on two-dimensional multi-mode interfaces. *J. Fluid Mech.* **928**, A37.

https://doi.org/10.1017/jfm.2022.213 Published online by Cambridge University Press

LIANG, Y., LIU, L., ZHAI, Z., SI, T. & WEN, C.-Y. 2020*a* Evolution of shock-accelerated heavy gas layer. *J. Fluid Mech.* **886**, A7.
LIANG, Y. & LUO, X. 2021*a* On shock-induced heavy-fluid-layer evolution. *J. Fluid Mech.* **920**, A13.
LIANG, Y. & LUO, X. 2021*b* Shock-induced dual-layer evolution. *J. Fluid Mech.* **929**, R3.
LIANG, Y. & LUO, X. 2022 On shock-induced light-fluid-layer evolution. *J. Fluid Mech.* **933**, A10.
LIANG, Y., ZHAI, Z., DING, J. & LUO, X. 2019 Richtmyer–Meshkov instability on a quasi-single-mode interface. *J. Fluid Mech.* **872**, 729–751.
LIANG, Y., ZHAI, Z., LUO, X. & WEN, C. 2020*b* Interfacial instability at a heavy/light interface induced by rarefaction waves. *J. Fluid Mech.* **885**, A42.
LINDL, J., LANDEN, O., EDWARDS, J., MOSES, E. & TEAM, N. 2014 Review of the national ignition campaign 2009–2012. *Phys. Plasmas* **21**, 020501.
LIU, L., LIANG, Y., DING, J., LIU, N. & LUO, X. 2018 An elaborate experiment on the single-mode Richtmyer–Meshkov instability. *J. Fluid Mech.* **853**, R2.
LUO, X., LIANG, Y., SI, T. & ZHAI, Z. 2019 Effects of non-periodic portions of interface on Richtmyer–Meshkov instability. *J. Fluid Mech.* **861**, 309–327.
LUO, X., LIU, L., LIANG, Y., DING, J. & WEN, C.Y. 2020 Richtmyer–Meshkov instability on a dual-mode interface. *J. Fluid Mech.* **905**, A5.
MANSOOR, M.M., DALTON, S.M., MARTINEZ, A.A., DESJARDINS, T., CHARONKO, J.J. & PRESTRIDGE, K.P. 2020 The effect of initial conditions on mixing transition of the Richtmyer–Meshkov instability. *J. Fluid Mech.* **904**, A3.
MESHKOV, E.E. 1969 Instability of the interface of two gases accelerated by a shock wave. *Fluid Dyn.* **4**, 101–104.
MEYER, K.A. & BLEWETT, P.J. 1972 Numerical investigation of the stability of a shock-accelerated interface between two fluids. *Phys. Fluids* **15**, 753–759.
MIKAELIAN, K.O. 1985 Richtmyer–Meshkov instabilities in stratified fluids. *Phys. Rev.* A **31**, 410–419.
MIKAELIAN, K.O. 1995 Rayleigh–Taylor and Richtmyer–Meshkov instabilities in finite-thickness fluid layers. *Phys. Fluids* **7** (4), 888–890.
MIKAELIAN, K.O. 1996 Numerical simulations of Richtmyer–Meshkov instabilities in finite-thickness fluid layers. *Phys. Fluids* **8** (5), 1269–1292.
MIKAELIAN, K.O. 1998 Analytic approach to nonlinear Rayleigh–Taylor and Richtmyer–Meshkov instabilities. *Phys. Rev. Lett.* **80**, 508–511.
MIKAELIAN, K.O. 2003 Explicit expressions for the evolution of single-mode Rayleigh–Taylor and Richtmyer–Meshkov instabilities at arbitrary Atwood numbers. *Phys. Rev.* E **67**, 026319.
MONTGOMERY, D.S., *et al.* 2018 Design considerations for indirectly driven double shell capsules. *Phys. Plasmas* **25** (9), 092706.
MORGAN, R.V., CABOT, W.H., GREENOUGH, J.A. & JACOBS, J.W. 2018 Rarefaction-driven Rayleigh–Taylor instability. Part 2. Experiments and simulations in the nonlinear regime. *J. Fluid Mech.* **838**, 320–355.
MORGAN, R.V., LIKHACHEV, O.A. & JACOBS, J.W. 2016 Rarefaction-driven Rayleigh–Taylor instability. Part 1. Diffuse-interface linear stability measurements and theory. *J. Fluid Mech.* **791**, 34–60.
NISHIHARA, K., WOUCHUK, J.G., MATSUOKA, C., ISHIZAKI, R. & ZHAKHOVSKY, V.V. 2010 Richtmyer–Meshkov instability: theory of linear and nonlinear evolution. *Phil. Trans. R. Soc.* A **368**, 1769–1807.
ORLICZ, G.C., BALAKUMAR, B.J., TOMKINS, C.D. & PRESTRIDGE, K.P. 2009 A Mach number study of the Richtmyer–Meshkov instability in a varicose, heavy-gas curtain. *Phys. Fluids* **21** (6), 064102.
ORLICZ, G.C., BALASUBRAMANIAN, S. & PRESTRIDGE, K.P. 2013 Incident shock Mach number effects on Richtmyer–Meshkov mixing in a heavy gas layer. *Phys. Fluids* **25** (11), 114101.
PENG, N., YANG, Y., WU, J. & XIAO, Z. 2021 Mechanism and modelling of the secondary baroclinic vorticity in the Richtmyer–Meshkov instability. *J. Fluid Mech.* **911**, A56.
PRESTRIDGE, K., VOROBIEFF, P., RIGHTLEY, P.M. & BENJAMIN, R.F. 2000 Validation of an instability growth model using particle image velocimtery measurement. *Phys. Rev. Lett.* **84**, 4353–4356.
RAYLEIGH, LORD 1883 Investigation of the character of the equilibrium of an incompressible heavy fluid of variable density. *Proc. Lond. Math. Soc.* **14**, 170–177.
RICHTMYER, R.D. 1960 Taylor instability in shock acceleration of compressible fluids. *Commun. Pure Appl. Maths* **13**, 297–319.
RIGHTLEY, P.M., VOROBIEFF, P. & BENJAMIN, R.F. 1997 Evolution of a shock-accelerated thin fluid layer. *Phys. Fluids* **9** (6), 1770–1782.
SADOT, O., EREZ, L., ALON, U., ORON, D., LEVIN, L.A., EREZ, G., BEN-DOR, G. & SHVARTS, D. 1998 Study of nonlinear evolution of single-mode and two-bubble interaction under Richtmyer–Meshkov instability. *Phys. Rev. Lett.* **80**, 1654–1657.

https://doi.org/10.1017/jfm.2022.213 Published online by Cambridge University Press

SOHN, S.I. 2003 Simple potential-flow model of Rayleigh–Taylor and Richtmyer–Meshkov instabilities for all density ratios. *Phys. Rev.* E **67**, 026301.

SUN, R., DING, J., ZHAI, Z., SI, T. & LUO, X. 2020 Convergent Richtmyer–Meshkov instability of heavy gas layer with perturbed inner surface. *J. Fluid Mech.* **902**, A3.

TAYLOR, G. 1950 The instability of liquid surfaces when accelerated in a direction perpendicular to their planes. I. *Proc. R. Soc. Lond.* A **201** (1065), 192–196.

TOMKINS, C.D., BALAKUMAR, B.J., ORLICZ, G., PRESTRIDGE, K.P. & RISTORCELLI, J.R. 2013 Evolution of the density self-correlation in developing Richtmyer–Meshkov turbulence. *J. Fluid Mech.* **735**, 288–306.

TOMKINS, C., KUMAR, S., ORLICZ, G. & PRESTRIDGE, K. 2008 An experimental investigation of mixing mechanisms in shock-accelerated flow. *J. Fluid Mech.* **611**, 131–150.

VANDENBOOMGAERDE, M., GAUTHIER, S. & MÜGLER, C. 2002 Nonlinear regime of a multimode Richtmyer–Meshkov instability: a simplified perturbation theory. *Phys. Fluids* **14** (3), 1111–1122.

VANDENBOOMGAERDE, M., MÜGLER, C. & GAUTHIER, S. 1998 Impulsive model for the Richtmyer–Meshkov instability. *Phys. Rev.* E **58** (2), 1874.

VELIKOVICH, A.L. & DIMONTE, G. 1996 Nonlinear perturbation theory of the incompressible Richtmyer–Meshkov instability. *Phys. Rev. Lett.* **76** (17), 3112.

VELIKOVICH, A. & PHILLIPS, L. 1996 Instability of a plane centered rarefaction wave. *Phys. Fluids* **8** (4), 1107–1118.

YANG, J., KUBOTA, T. & ZUKOSKI, E.E. 1993 Application of shock-induced mixing to supersonic combustion. *AIAA J.* **31**, 854–862.

ZHAI, Z., ZOU, L., WU, Q. & LUO, X. 2018 Review of experimental Richtmyer–Meshkov instability in shock tube: from simple to complex. *Proc. Inst. Mech. Engng* C **232**, 2830–2849.

ZHANG, Q. 1998 Analytical solutions of Layzer-type approach to unstable interfacial fluid mixing. *Phys. Rev. Lett.* **81** (16), 3391.

ZHANG, Q., DENG, S. & GUO, W. 2018 Quantitative theory for the growth rate and amplitude of the compressible Richtmyer–Meshkov instability at all density ratios. *Phys. Rev. Lett.* **121** (17), 174502.

ZHANG, Q. & GUO, W. 2016 Universality of finger growth in two-dimensional Rayleigh–Taylor and Richtmyer–Meshkov instabilities with all density ratios. *J. Fluid Mech.* **786**, 47–61.

ZHANG, Q. & SOHN, S.I. 1997 Nonlinear theory of unstable fluid mixing driven by shock wave. *Phys. Fluids* **9**, 1106–1124.

ZHOU, Y. 2017*a* Rayleigh–Taylor and Richtmyer–Meshkov instability induced flow, turbulence, and mixing. I. *Phys. Rep.* **720–722**, 1–136.

ZHOU, Y. 2017*b* Rayleigh–Taylor and Richtmyer–Meshkov instability induced flow, turbulence, and mixing. II. *Phys. Rep.* **723–725**, 1–160.

ZHOU, Y., CABOT, W.H. & THORNBER, B. 2016 Asymptotic behavior of the mixed mass in Rayleigh–Taylor and Richtmyer–Meshkov instability induced flows. *Phys. Plasmas* **23** (5), 052712.

ZHOU, Y., CLARK, T.T., CLARK, D.S., GLENDINNING, S.S., SKINNER, A.A., HUNTINGTON, C., HURRICANE, O.A., DIMITS, A.M. & REMINGTON, B.A. 2019 Turbulent mixing and transition criteria of flows induced by hydrodynamic instabilities. *Phys. Plasmas* **26** (8), 080901.

ZHOU, Y., *et al.* 2021 Rayleigh–Taylor and Richtmyer–Meshkov instabilities: a journey through scales. *Physica* D **423**, 132838.

https://doi.org/10.1017/jfm.2022.213 Published online by Cambridge University Press